

pubs.acs.org/acssensors Article

# Sensitive Detection of Perfluoroalkyl Substances Using MXene—AgNP-Based Electrochemical Sensors

Reem Khan, Zihni Onur Uygun, Daniel Andreescu, and Silvana Andreescu\*



Cite This: https://doi.org/10.1021/acssensors.4c00776



ABSTRACT: Per- and polyfluoroalkyl substances (PFAS) pose a significant threat to the environment due to their persistence, ability to bioaccumulate, and harmful effects. Methods to quantify PFAS rapidly and effectively are essential to analyze and track contamination, but measuring PFAS down to the ultralow regulatory levels is extremely challenging. Here, we describe the development of a low-cost sensor that can measure a representative PFAS, perfluorooctanesulfonic acid (PFOS), at the parts per quadrillion (ppq) level within 5 min. The method combines the ability of PFOS to bind to silver nanoparticles (AgNPs) embedded within a fluorine-rich Ti<sub>3</sub>C<sub>2</sub>-based multilayered MXene, which provides a large surface area and accessible binding sites for direct impedimetric detection. Fundamentally, we show that MXene–AgNPs are capable of binding PFOS and other long-chain PFAS compounds, though the synergistic action of AgNPs and MXenes via electrostatic and F–F interactions. This binding induced concentration-dependent changes in the charge-transfer resistance, enabling rapid and direct quantification with extremely high sensitivity and no response to interferences. The sensor displayed a linear range from 50 ppq to 1.6 ppt (parts per trillion) with an impressively low limit of detection of 33 ppq and a limit of quantification of 99 ppq, making this sensor a promising candidate for low-cost screening of the PFAS content in water samples, using a simple and inexpensive procedure.

KEYWORDS: per- and polyfluoroalkyl, impedance, MXene, silver nanoparticle, chronoimpedance

er- and polyfluoroalkyl substances (PFAS) are a group of synthetic chemicals that have gained significant attention due to their prevalence in the environment and adverse health effects. These substances have been used in various industrial and consumer applications, such as aqueous film-forming foam (AFFF), nonstick coatings, and water repellents.<sup>2</sup> PFAS are highly resistant to degradation,<sup>3</sup> which has led to their widespread presence in soil, water, air, and even food sources. A recent study conducted by the Center for Disease Control and Prevention (CDC) has indicated that a significant portion of the U.S. population has been exposed to PFAS. Exposure to PFAS is linked to chronic diseases such as liver damage, immune system dysfunction, developmental issues, and an increased risk of cancer.<sup>5</sup> Among the different types of PFAS, the "long-chain" perfluoroalkyl carboxylic acids  $(C_nF_{2n}+COOH, n \ge 7)$  and perfluoroalkyl sulfonic acids  $(C_nF_{2n} + SO_3H, n \ge 6)$  are of particular concern.<sup>6</sup> In response to growing concerns, the U.S. Environmental Protection Agency (EPA) revised (March 2023) the initial PFAS health advisory limit of 70 ppt in drinking water for a combined perfluorooctanoic acid (PFOA) and perfluorooctanesulfonic acid (PFOS) content. The new recommendation refers to six

different PFAS including long-chain (PFOS, PFOA, and perfluorononanoic acid (PFNA)) and short-chain (perfluorobutanesulfonic acid (PFBS), perfluorohexanesulfonic acid (PFHxS), perfluorohexanoic acid (PFHxA), and hexafluoropropylene oxide dimer acid (HFPO-DA or GenX)) compounds. The new enforceable limits (April 2024) are 4 ppt for PFOA and PFOS as individual contaminants and 1 (Unitless Hazard Index) for PFHxS, PFNA, PFBS, and GenX as a mixture. These updated levels serve as a cautionary indication that even ultratrace levels of PFOA and PFOS in water may have potential negative effects. Nevertheless, the analysis of these substances at such low concentrations is challenging and requires the development of rapid, affordable,

 Received:
 April 3, 2024

 Revised:
 May 22, 2024

 Accepted:
 May 27, 2024



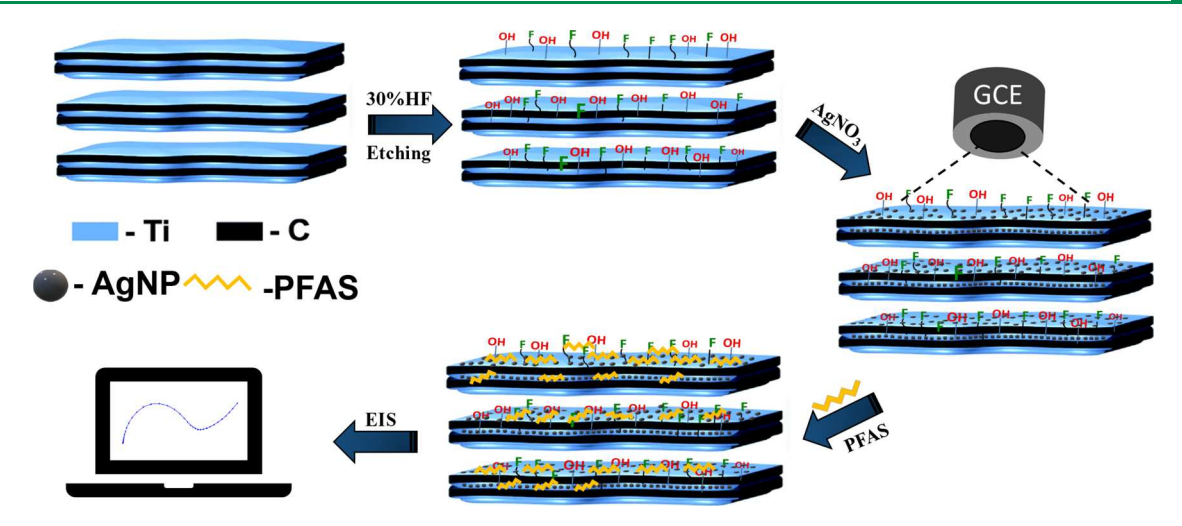


Figure 1. MXene-AgNP detection concept for PFAS showing the assembly of the AgNPs and PFAS binding sites within the multilayered  $Ti_3C_2$  MXenes. PFAS binding occurs synergistically on the AgNPs and through F-F interaction with the F-rich MXene.

and ultrasensitive detection methods to address the increased testing needs.

The standard EPA methods for the detection of PFAS are based on chromatography coupled with mass spectrometry (LC/MS/MS) and EPA methods 537.1 and 533. Although these methods are sensitive and accurate, they are costprohibitive and lack portability. Most laboratories do not have the instrumentation and trained personnel to measure PFAS and fulfill the need for large-scale monitoring and testing. Several approaches to developing portable and inexpensive methods have been reported. These include spectrophotometric detection with fluorescence probes<sup>8</sup> or plasmonic nanoparticles,<sup>9</sup> total organic fluorine analysis,<sup>10</sup> electrochemical sensors,<sup>11</sup> and metal—organic frameworks (MOFs) as PFAS sorption media. 12 While these platforms have the ability to detect PFAS, they lacked sensitivity, in some cases by several orders of magnitude (ppm/ppb vs ppt), and are prone to interferences from the coexisting compounds. Moreover, their ability to measure PFAS in real-world samples has not been demonstrated. The coexistence of ions, organic matter, and various surfactants can interfere in readings, affecting the accuracy and specificity of measurements. 13 Several electrochemical studies 11b,14 using molecularly imprinted polymer (MIP)-based sensors have demonstrated promising analytical performances for PFOS analysis, including the initial work from Ugo's group with a limit of detection (LOD) of 0.04 nM (20 ppt)<sup>15</sup> and the study of effects generated by the presence of possible interfering compounds by Dick's group. 16 A recent work using similarly designed MIP-based electrodes and ambient oxygen or electrogenerated dioxygen molecules 18 as mediators demonstrated indirect detection for PFOS with lower LODs (~1 ppt) as well as measurements of GenX also with a very low LOD (0.834 ppt). 19 These new developments demonstrate the potential of electrochemical methods to reach the level of sensitivity required by the extremely low regulatory limits for PFAS.<sup>7,20</sup>

We recently demonstrated the ability of citrate-coated AgNPs to interact with long-chain sulfonated PFAS, such as PFOS, by selective displacement of the citrate with the sulfonate group of the PFOS, followed by a slight aggregation through F–F interactions of the adsorbed PFOS. These results demonstrated that colloidal AgNPs can be used as probes to indirectly quantify PFOS by measuring changes in

the electron transfer at the NP surface upon PFOS binding. Measurements were carried out using single-particle collision electrochemistry, which is sensitive but not practical for realworld measurements. Here, we use the selective binding of long-chain PFAS to AgNPs to develop a portable nanosensor platform for these compounds. To fabricate the sensor, the AgNPs were embedded within Ti<sub>3</sub>C<sub>2</sub>-based multilayered MXenes which provides a conductive supporting matrix that can act as a transduction platform to stabilize and homogeneously deposit the AgNPs. The sensing principle is illustrated in Figure 1. MXenes are two-dimensional (2D) lamellar-structured nanomaterials produced by a top-down etching process of a MAX phase using acidic solutions that contain fluoride ions. The MAX phase represents a class of hexagonal carbides and nitrides having a general formula of  $Mn_{+1}AX_n$  (n = 1-4), where M is an early transitional metal (Sc, Ti, Cr, Zr, Mo, Nb, Hf, and Ta), A is A (mainly III,IV)group element (Al, Si, Cd, Ge, As, and Pb), and X is C, N, or CN.<sup>22</sup> The surface functionalities of the resulting MXene are mainly OH, -O, and -F. MXenes have gained significant attention due to their hydrophilicity, metal-like electrical conductivity, high surface area, and tunable surface chemistry,<sup>23</sup> which enabled their use in diverse applications such as energy storage, catalysis, sensing, and environmental remediation. 24 MXenes have also been used as adsorbents for heavy metals and<sup>25</sup> organic compounds such as azithromycin, bacitracin, tetracycline, and other contaminants including PFAS<sup>26–28</sup> and have shown promise in the photocatalytic degradation of organic pollutants.29

Herein, we demonstrate the ability of Ti<sub>3</sub>C<sub>2</sub> MXene decorated with AgNPs (MXene–AgNPs) to serve as a sensing material for PFOS. In addition to their high surface area and conductivity, Ti<sub>3</sub>C<sub>2</sub> MXenes have fluorine functionalities which may favor fluorophillic interactions with PFAS, similar to those reported for the separation of fluorous compounds by reverse fluorous solid-phase extraction<sup>30</sup> and those for PFOA capture by cationic fluorinated sorbents<sup>31</sup> or by fluorine-functionalized MOFs.<sup>32</sup> Such interactions could act synergistically with the AgNPs and ultimately provide multibinding sites, enhancing the detection sensitivity. To develop the sensor, we first determined the optimal conditions for the MXene–AgNP synthesis and deposition on electrodes and then used electrochemical impedance spectroscopy (EIS)<sup>33</sup> to quantify

PFOS binding, providing ultrasensitive ppq-level detection with a total analysis time of 5 min. We further demonstrate that our MXene—AgNPs are selective toward PFOS and show very low response to interferences such as surfactants with a similar structure but lacking F—C bonds and no response to ions. We also demonstrate that the sensor can measure several other long-chain PFAS substances. Together, these results establish the use of MXene—AgNPs as a sensing platform for long-chain PFAS and demonstrate potential applicability for the detection of these emerging contaminants in environmental water samples.

# MATERIALS AND METHODS

Chemicals. All chemicals were purchased from commercial sources and used without further purification. The MAX-phase titanium aluminum carbide powder (Ti<sub>3</sub>AlC<sub>2</sub>, purity 99%) was purchased from Nanoshel LLC. Hydrofluoric acid (HF), sodium chloride (NaCl), potassium fluoride (KF), potassium ferricyanide [K<sub>3</sub>Fe(CN)<sub>6</sub>], sodium sulfate (Na<sub>2</sub>SO<sub>4</sub>), octanoic acid (OA), 1octanesulfonic acid sodium salt (OSA), perfluorooctanoic acid (PFOA), perfluorooctanesulfonic acid potassium salt (PFOS), perfluorononanesulfonic acid sodium salt (PFNS), hexafluoropropylene oxide dimer acid (HFPO-DA or GenX), perfluorobutanesulfonic acid (PFBS), humic acid (HA), and 4-docecylbenzenesulfonic acid (4-DBS) were purchased from Sigma-Aldrich. Perfluorononanoic acid (PFNA) and perfluorohexanoic acid (PFHxA) were purchased from TCI America. Perfluorobutanoic acid (PFBA) was acquired from Acros Organics. Sodium phosphate monobasic (NaH<sub>2</sub>PO<sub>4</sub>) anhydrous was purchased from Spectrum Chemical; potassium iodide (KI), acetonitrile, and ethanol from Fisher Scientific; and silver nitrate (AgNO<sub>3</sub>) from Alfa Aesar. Two samples of industrial wastewater were obtained from a wastewater treatment plant.

MXene and MXene-AgNP Synthesis and Characterization. Ti<sub>3</sub>C<sub>2</sub> MXene was synthesized via wet chemical etching from the Ti<sub>3</sub>AlC<sub>2</sub> MAX-phase precursor as previously reported.<sup>34</sup> Briefly, 1 g of Ti<sub>3</sub>AlC<sub>2</sub> was gradually added to 30% HF etchant solution over the course of 5 min in a polypropylene beaker. This solution was stirred for 16 h at room temperature (RT) using a Teflon magnetic stirrer. The concentrated HF selectively etched the Al layer out of the Ti<sub>3</sub>AlC<sub>2</sub> precursor. The resulting precipitate was washed several times using 40 mL of deionized (DI) water with repeated centrifugation at 3500 rpm for 5 min, and the acidic supernatant was removed. The washing step was repeated until the pH reached 6.5. Afterward, the precipitate was filtered through a vacuum funnel holding a filter membrane (47 mm diameter and 0.45  $\mu$ m pore size) from Millipore, followed by overnight drying under vacuum at 80 °C. The synthesis of AgNPs within MXene was performed by in situ reduction of silver nitrate.<sup>35</sup> Briefly, 0.1 g of MXene was dispersed in 80 mL of DI water and kept in an ultrasonic bath for 30 min. In a separate vial, 15.77 mg of AgNO<sub>3</sub> was dissolved in 10 mL of DI water and injected dropwise into the MXene dispersion under vigorous stirring to reduce AgNO3 to AgNPs. The composite was kept in the ultrasonic bath for 10 min, centrifuged, and washed three times with DI water, followed by vacuum drying at 80 °C for 3 h. This composite corresponds to a 10% Ag content (MXene-AgNPs10). To optimize the amount of AgNPs, two other different composites with Ag content of 20 wt % (39.7 mg of AgNO<sub>3</sub>) identified as MXene-AgNPs20 and 40 wt % (79.4 mg of AgNO<sub>3</sub>)-MXene-AgNPs40 were prepared using the same procedure. To characterize the PFOS adsorption to the resulting materials, 0.5 g of MXene or MXene-AgNPs was separately incubated with 1 ppm of PFOS for 1 h at RT. The solid was separated by centrifugation, washed three times with DI water, and collected using the same vacuum filtration assembly, followed by overnight drying in a vacuum oven at 80 °C. These samples were characterized by using spectroscopic and thermogravimetric methods, as described in the characterization section.

Instrumentation and Electrochemical Characterization. Scanning electron microscopy (SEM) images were acquired with a JSM 7900 scanning electron microscope (JEOL) having attached an Aztek EDS detector (Oxford Instrument) to perform the energydispersive X-ray spectroscopy (EDS) analysis. The powder X-ray diffraction (PXRD) measurements were carried out with a Malvern PANalytical X'Pert PRO MRD diffractometer on a Si crystal zero background holder. Fourier transform infrared (FTIR) spectroscopy absorption spectra were recorded with a Nicolet iS-10 (Thermo Scientific) spectrophotometer. The solid-state UV-vis measurements were performed with a Cary 4000 UV-vis spectrophotometer incorporating an integrated sphere from Agilent. Thermal stability was investigated by thermogravimetric analysis (TGA) using a Q50 thermal analyzer (TA Instruments). The thermogravimetry-mass spectrometry (TGA-MS) tests were performed with a Seiko Exstar TG/DTA 6200 thermoanalyzer coupled with a Pfeiffer Vacuum ThermoStar GSD 301 T2 mass spectrometer, under helium atmosphere. For these tests, samples were placed on a Pt pan and heated up to 800 °C with a heating rate of 10 °C/min. The electrochemical measurements were performed with a CHI920 potentiostat (CH Instruments, USA) using a 3 mm glassy carbon electrode (GCE) as the working electrode (MF-2012), platinum wire (MW-1032) as the counter electrode, and Ag/AgCl electrode (3 M KCl) as the reference electrode (MF-2056), all from BASi Inc. Prior to use, the GCE was physically cleaned on a polish pad with alumina slurry (0.05  $\mu$ m) and separately sonicated in ethanol and water for 2 min. For validation purpose, the real samples were also analyzed with the LC/MS/MS standard method using a UPLC-MS-MS system (Thermo Scientific, Vanquish-TSQ ALTIS) equipped with an Acquity HSS T3 column (2.1 mm  $\times$  100 mm, 1.8  $\mu$ m). The tests were performed at the Center for Air and Aquatic Resources Engineering and Sciences (CAARES) at Clarkson University, a certified laboratory for PFAS analysis by the Department of Defense, Environmental Laboratory Accreditation Program (DoD ELAP).

Sensor Fabrication and EIS Measurements. To fabricate the sensors, 2 µL of an ink consisting of 2 mg of either MXene or MXene-AgNP composite, previously dispersed in 2 mL of acetonitrile, was drop-casted on the surface of a GCE and dried at RT. Next, the electrodes were immersed in PFOS solutions, with concentrations ranging between 50 ppq and 1.6 ppt. After 5 min of incubation, the electrodes were rinsed with DI water and transferred into the electrochemical cell. EIS and chronoimpedance were used to characterize the electrode surface and evaluate the changes in the electron transfer resistance (Ret) upon PFAS binding. The electrochemical cell (5 mL) contains 5 mM  $Fe(CN)_6^{3-/4}$  redox probe solution prepared in a phosphate-buffered saline (PBS) solution (100 mM KCl and 50 mM NaH<sub>2</sub>PO<sub>4</sub>) at pH = 7. The EIS characterization was carried out at 180 mV DC and 10 mV AC potential and the frequency between 10,000 and 0.05 Hz.<sup>36</sup> The measurements were repeated for several concentrations of PFOS to build a calibration curve. All measurements were performed in at least triplicate with independently prepared electrodes. To establish the selectivity and specificity of measurements, a series of PFAS compounds including sulfonate and carboxylate forms, as well as several possible interfering substances, including compounds of similar length as the tested PFAS but lacking C-F bonds, organic matter (HA), and surfactants (4-DBS) were analyzed using the same procedure. The chronoimpedance measurements were carried out in a 5 mL electrochemical cell containing PBS solution (pH 7) with different PFOS concentrations  $(1 \div 10 \text{ ppt}).$ 

# ■ RESULTS AND DISCUSSION

Physicochemical Characterization of MXene and MXene–AgNPs. To ensure uniform deposition of AgNPs within the MXene, the AgNPs were synthesized in situ by the reduction of silver ions in the presence of MXene. The Ag ion reduction in the MXene  $(Ti_3C_2(OH)_{0.8}F_{1.2})$  solution is associated with the presence of low-valence Ti (Ti-OH) that can act as a reducing agent for the silver ions,  $^{35,37}$  thus enabling the growth of AgNPs when Ag ions are exposed to the

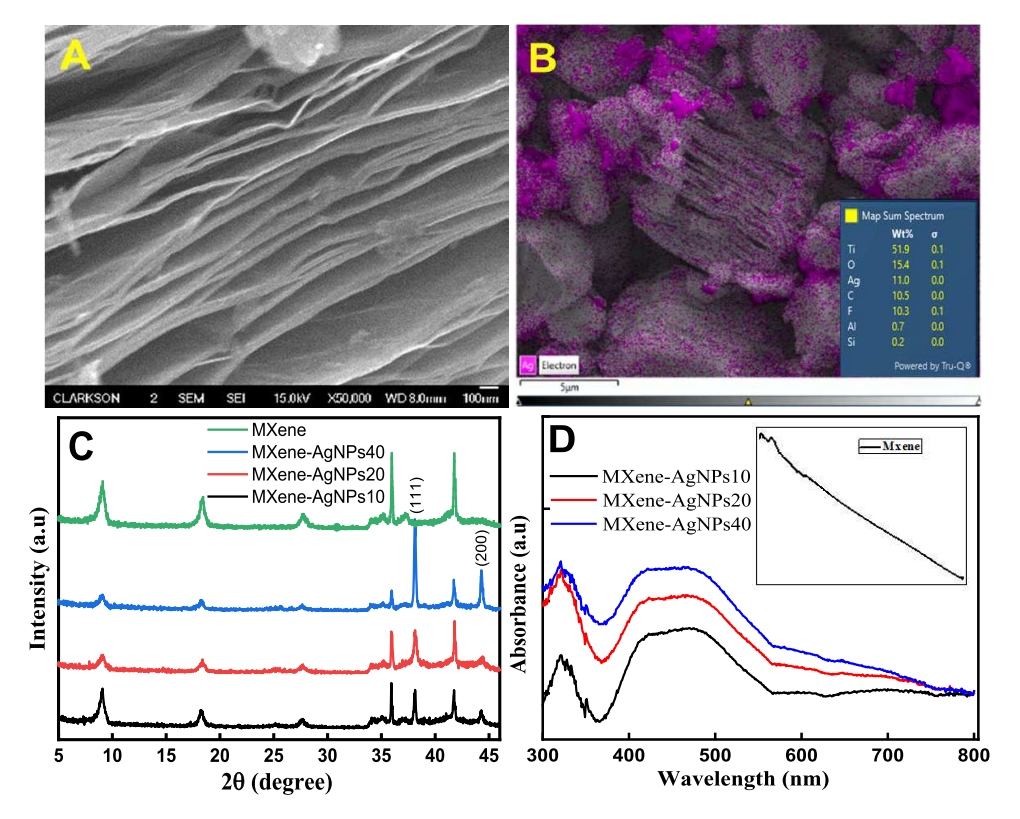


Figure 2. (A) SEM image of Ti<sub>3</sub>C<sub>2</sub> MXene; (B) SEM image of MXene–AgNPs20 overlapped with Ag EDS mapping; (C) PXRD pattern on MXene and MXene–AgNPs (stacked) prepared with 10, 20, and 40% Ag content (MXene–AgNPs10, MXene–AgNPs20, and MXene–AgNPs40), and (D) solid-state UV–vis spectra of MXene (inset) and the MXene–AgNP composites.

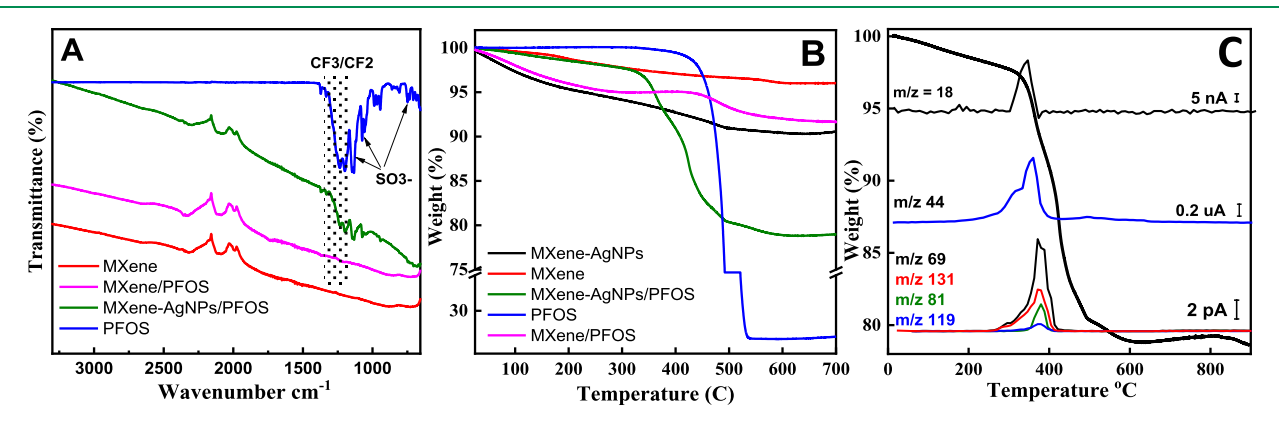


Figure 3. (A) FTIR spectra of PFOS, bare MXene, and MXene and MXene–AgNPs10 exposed to 1 ppm of PFOS, (B) resultant TGA curves of these materials, and (C) combined TGA–MS profiles of MXene–AgNPs10.

MXene. The resulting MXene—AgNP composite was first characterized to confirm the layered structure, identify the presence of surface functional groups, and demonstrate the presence of AgNPs. The SEM of MXene synthesized in the first step (Figure 2A) confirms the successful etching of the Al layer out of the  $Ti_3AlC_2$  MAX phase by the strong HF solution and formation of 2D nanochannels. Next, the SEM image along with the EDS mapping of the MXene—AgNP composite confirms the in situ reduction and formation of AgNPs (Figure 2B) with no alteration of the multilayered MXene structure. The average diameter of AgNPs attached to the 2D MXene surface is ~180 nm (Figure S1 in the Supporting Information, SI). The PXRD pattern (Figure 2C) also confirms the presence of AgNPs (JCPDS file 04–0783) by showing the two major diffraction peaks indexed as Ag(111) and Ag(200) at 2θ of

38.2 and 44.2 degrees, respectively. Although the patterns are stacked for better visibility, the intensity of Ag(111) and Ag(200) reflections increased as the silver content increased, demonstrating the formation of controllable amounts of crystalline face-centered cubic (fcc) AgNPs on MXene. The peak sharpness increased with an increasing concentration of Ag, indicating an improved crystallinity. Additionally, no shift in the MXene 002 peak position at 9° was observed which suggests no intercalation of AgNPs inside the MXene layers. It is known that AgNPs possess a strong surface plasmon resonance, with characteristic absorption peaks between 400 and 450 nm depending on the NP size and shape.<sup>39</sup> We thus used UV—vis spectroscopy to further confirm the presence of the AgNPs. A broad absorption peak between 400 and 500 nm appeared in the solid-state UV—vis spectra (Figure 2D), with

the peak intensity increasing with the increase of Ag content from 10 to 40%, which indicates the presence of polydisperse AgNPs. The presence of AgNPs in all three composites in a concentration-dependent manner was also confirmed by SEM and elemental mapping (Figure S2) as well as EDS analysis (Figure S3). With these measurements, we demonstrate the successful incorporation of AgNPs and the formation of hybrid structures having the NPs firmly anchored on the MXene surface.

Following the confirmation of MXene-AgNP structure and morphology, we characterized the interaction of PFOS with MXene and MXene-AgNPs. To establish the binding mechanism, the composites were first evaluated by FTIR spectroscopy before and after exposure to assess the presence of the PFOS functional groups, particularly the sulfonate and CF3/CF2 groups. Before analysis, samples were washed to remove the weakly adsorbed PFOS. As expected, the FTIR spectra of MXene-AgNPs exposed to PFOS show the presence of sulfonate vibration peaks at 600-750, 1000-1075, and 1120-1170 cm<sup>-1</sup> and the CF3/CF2 peaks at 1200-1350 cm<sup>-1</sup> (Figure 3A). This indicates that a significant amount of PFOS is adsorbed onto their surface. The same peaks, with a significantly lower intensity, appeared on the spectrum of MXene exposed to PFOS under the same conditions, indicating a much lower PFOS content. The adsorbed PFOS was further quantified by TGA measurements, which provide mass loss profiles of the MXene with or without AgNPs, before and after exposure to PFOS (Figure 3B). The PFOS decomposition occurred between 400 and 500 °C with 80% weight loss. Neither MXene nor MXene-AgNPs alone showed mass degradation at this temperature range. After exposure to PFOS, the MXene-AgNPs10 showed a significant weight loss (~20%) between 300 and 400 °C assigned to PFOS decomposition. The temperature shift toward a lower temperature range can be attributed to the potential catalytic activity of AgNPs, which can promote the decomposition of PFOS and lower its decomposition temperature. 40 In this case, the AgNPs might provide active sites that facilitate the breakdown of surface-attached PFOS at lower temperatures as compared to that of pure PFOS. By comparison, when AgNPs are not present, a very small weight loss (~5%) was observed between 500 and 700 °C, indicating the presence of a very small amount of PFOS on the MXene. These results demonstrate enhanced PFOS adsorption by the addition of AgNPs to the MXene.

The presence of PFOS onto MXene–AgNPs10 was further confirmed by TGA MS analysis (Figure 3C). The TGA weight loss profile shows three successive decomposition steps between 300 and 600 °C with a mixture of fragments having m/z values of 18, 44, 69, 81, 119, and 131. The fragments at m/z 18 and 44 can be associated with the elimination of water and carbon dioxide. The weight loss between 400 and 600 °C generated gaseous products related to various fluorinated fragments including CF<sub>3</sub> (m/z=69), C<sub>2</sub>F<sub>3</sub> (m/z=81), and C<sub>2</sub>F<sub>5</sub> (m/z=119). The appearance of these fragments in MS confirms the adsorption of PFOS onto the MXene–AgNP surface.

**Electrochemical Characterization and Optimization of the Sensor.** Due to its sensitivity, we used EIS as an electrochemical technique to characterize the electrode surface and quantify the binding of PFAS. EIS is known for its ability to provide a direct and fast analysis of interfacial chemical reactions with high sensitivity over a range of frequencies.<sup>33</sup>

The GCE was used as the sensing platform to immobilize the MXene–AgNPs, and 5 mM Fe(CN) $_6^{3-/4-}$  prepared in PBS (pH 7) was used as the redox probe. To avoid the dissolution of the AgNPs in acidic pH or formation of an oxide layer on the AgNP surface at basic pH that will hinder the interaction with PFOS, a pH of 7 was used for all tests, which is also representative for water samples. The EIS curves (Nyquist plots) start very close to the origin, indicating excellent conductivity and a behavior characterized by a well-defined electron-transfer resistance ( $R_{\rm et}$ ) and Warburg impedance, as illustrated by the circuit model in Figure 4A. These elements

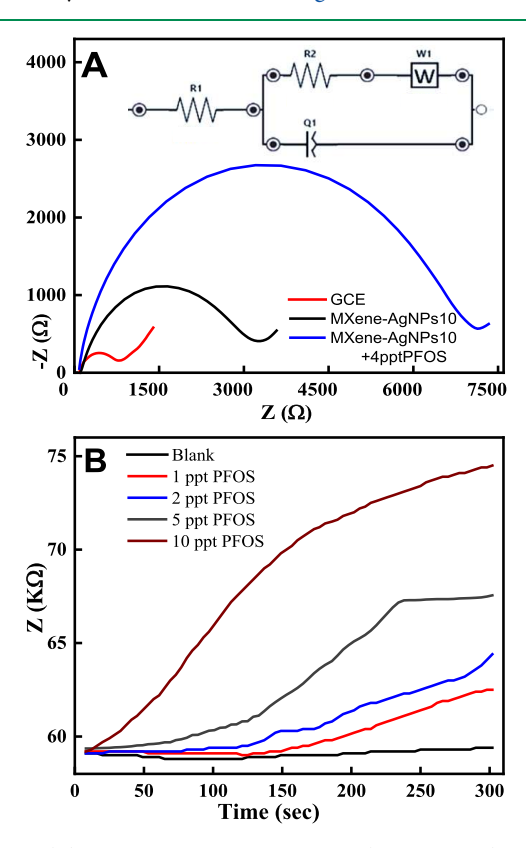
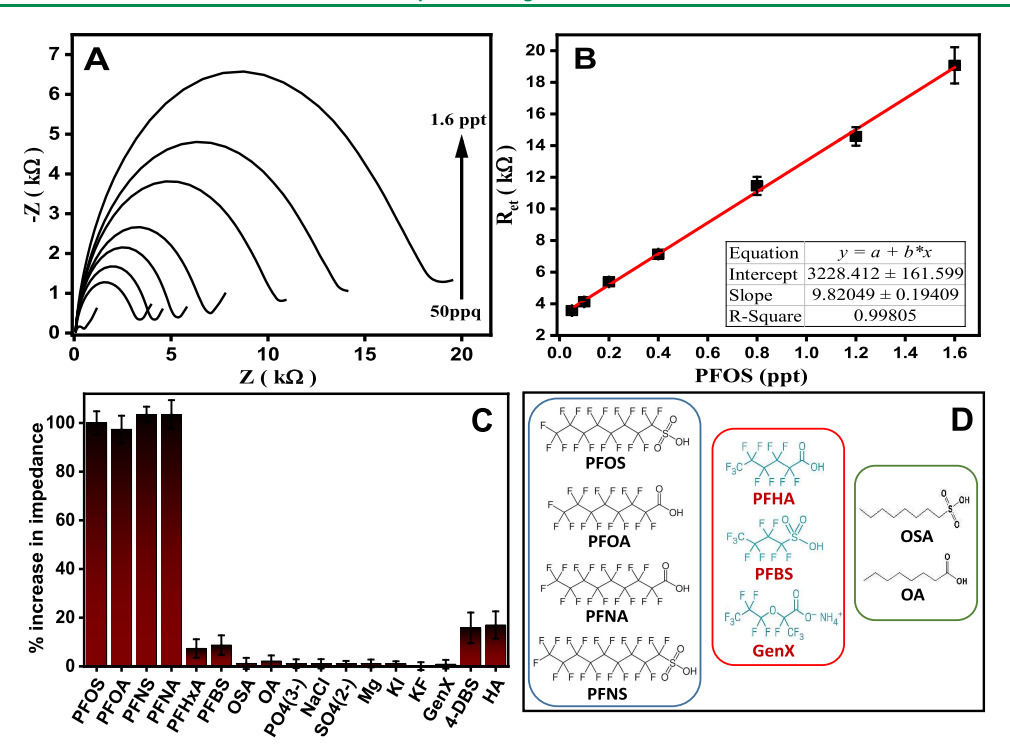


Figure 4. (A) Impedimetric EIS responses (Nyquist plot) and EIS recording of a Randles circuit including a Warburg element (inset) showing EIS changes measured at bare and MXene–AgNPs10-modified GCE before and after exposure to 4 ppt PFOS and (B) chronoimpedimetric detection using MXene–AgNPs10-modified GCE showing concentration-dependent changes upon exposure to parts per trillion level PFOS concentrations.

represent the solution resistance  $(R_1)$ , electrode surface impedance  $(R_{et} \text{ or } R_2)$ , and constant phase element as the double-layer electrical charge of the nanocomposite surface, and W is Warburg impedance. 42 The EIS signal was improved by lowering the resistance of the redox probe by adding KCl, and  $R_1$  shows an insignificant contribution from the solution resistance. To characterize PFAS binding, we used a constant phase element (Q) in the circuit model to quantify the nonhomogeneous/multilayer electrical charges at the electrode surface induced by the deposition of the MXene-AgNPs. Therefore, the EIS curves were fitted to the equivalent circuit, which includes the constant phase element. Upon the deposition of MXene-AgNPs, the diameter of the semicircle slightly increased, indicating changes in  $R_{\rm et}$  at the GCE. Upon exposure to a low concentration of PFOS (4 ppt), a significantly higher charge-transfer resistance was obtained,



**Figure 5.** (A) Nyquist plots of MXene–AgNPs10/GCE with different concentrations of PFAS carried out in 5 mM Fe(CN) $_6^{3-/4-}$  solution containing 0.1 M KCl and 50 mM NaH $_2$ PO $_4$ . The frequency ranges from 0.05 Hz to 10 kHz. (B) Calibration curve showing impedance vs PFOS concentration. (C) Sensor response for 1 ppt of various PFAS including PFOS, PFOA, PFNS, PNNA, PFHA, PFB, GenX, fluorine-free compounds with structural similarities: OSA and OA, and 1 ppm of several salts, including PO $_4^{3-}$ , NaCl, SO $_4^{2-}$ , Mg, KI, KF, as well as organic matter (HA) and surfactant (5-DBS). (D) Chemical structure of the tested compounds.

seen by the increased diameter of the semicircle, while the Warburg impedance dominancy decreased. This significant change induced by the presence of PFOS with contribution from the higher repulsion between the redox probe and the MXene-PFOS layer of increased hydrophobicity after PFOS attachment to AgNPs indicates that this can be used to measure PFOS. Such significant changes seen at a very low concentration suggest that this method can reach detection capabilities close to the currently EPA advisory PFOS limit in drinking water (4 ppt). Excluding the time needed to prepare the electrode, using this approach, the analysis can be completed within 5 min, which includes both the incubation of the modified electrode with the sample and the EIS measurement. Since the house of the GCE is Kel-F, a chemically inert F-based material below 60 °C (according to the manufacturer data), we have evaluated the possibility of a transfer of the F-content to the electrode surface area during measurements. The blank test with a GCE immersed for 25 min in measurement buffer (5 times higher than the analysis time) in the absence of PFOS shows no quantifiable difference in impedance, indicating that the leaching of F-content from the electrode housing to the surface area is practically zero. To further confirm this assumption and also evaluate the possible nonspecific adsorption, an additional control experiment was performed in which the bare GCE was incubated for 30 min in 1 ppt PFOS solution (clearly higher than a possible F transfer). The results, as illustrated in Figure S4A, showed practically no effect on the impedance spectra for the blank GCE as compared with the MXene-AgNPs/GCE, demonstrating no PFOS adsorption on the bare electrode.

To evaluate the ability of the method to quantitatively measure PFOS, we determined the changes in the electrode-

transfer resistance at the MXene-AgNP electrode for concentrations ranging from 1 to 10 ppt. Chronoimpedance was used in these tests to determine the sensitivity of the method for different concentrations and identify the optimal binding time of PFOS to the electrode surface. Notably, the assessment of the electrode surface resistance was conducted through nonfaradaic detection, which differs from a conventional electron-transfer resistance analysis. As shown in Figure 4B, the binding kinetics exhibited a direct correlation between the impedance changes, Z, and increasing PFOS concentrations. Specifically, at low concentrations such as 1 or 2 ppt, a measurable response was seen after 150 s, progressively increasing over time and demonstrating the capability of this method to measure extremely low levels of PFOS in a very short time. The association constant  $(K_A)$  and the number of binding sites (BS)<sub>0</sub> can be calculated by fitting the experimental data into a Langmuir isotherm model (Figure S4B) according to eq 1, $^{16}$  where  $Z_0$  and Z are the impedance values in the absence and presence of PFOS, respectively. The heterogeneity index (m) refers to the distribution type of the binding sites over the surface and varies from 1 (homogeneous) to 0 (heterogeneous). This model assumes a monolayer arrangement of PFAS molecules over the surface, expected as the PFOS concentration is very low (ppt).

$$Z - Z_0 = \frac{(BS)_0 K_A [PFOS]^m}{1 + K_A [PFOS]^m}$$
(1)

The  $K_{\rm A}$  value calculated from the best fit of the Langmuir isotherm model was  $2.00 \times 10^{10} \,\mathrm{M}^{-1}$ , the maximum number of binding sites was  $0.29 \times 10^6$ , and m close to 1 (~0.94), confirming a high affinity of PFOS for the binding sites and

homogeneous distribution of the binding sites, close to that reported for PFOS analysis using MIPs. 15

To optimize the system, we evaluated the response of the sensor as a function of AgNP content in the MXene composite, which is expected to influence the binding and indirectly affect the method sensitivity. In this hybrid configuration, the AgNPs facilitate electrostatic attraction of the negatively charged sulfonate groups, while MXene effectively engages with the fluorinated groups. Therefore, achieving the right balance between the two materials is important for optimal binding efficiency. Figure S5 in SI shows the EIS spectra for three different MXene-AgNP composites prepared with different Ag contents (10, 20, and 40%), incubated with the same concentration of PFOS (1 ppt). Interestingly, the highest change was seen for the composite prepared with 10% Ag, while increasing the Ag content had an opposite effect. This can be explained by AgNP agglomeration (reducing the surface area) and blocking of the MXene fluorine binding sites, reducing the availability for F-F interactions. Indeed, the elemental analysis of the three MXene-AgNP materials indicates reduced levels of F in the composites of 40 and 20% Ag compared with the one of 10% Ag content (Figure S3). Thus, all experiments to characterize the analytical performance of the sensor were performed with the optimal MXene-AgNP composite containing 10% Ag.

Analytical Performance of the PFAS Sensor. To demonstrate the synergistic effect of the hybrid MXene-AgNPs, we measured the electron-transfer resistance  $(R_{et})$ obtained by fitting the acquired EIS data to the equivalent circuit model, as shown in Figure 4, for different concentrations of PFOS. This approach enabled us to extract insights into the concentration-dependent changes in  $R_{et}$  and develop a calibration curve based on the correlation between impedance changes and concentrations. Figure 5A,B shows the evolution of impedance responses for PFOS concentrations ranging between 50 ppg and 1.6 ppt. The numerical EIS fitting results (average values from at least n = 3 electrodes) are provided in Table S1. A linear range was established for these concentrations with a linear equation y = 9.82x + 3228, where 'y' denotes the calculated impedance and 'x' the concentration of PFOS. The high coefficient of regression  $(R^2 = 0.9980)$  indicates a strong correlation in the sensing responses and a robust and substantial association between the binding interactions of PFOS and the sensor surface. The limit of detection (LOD) and limit of quantification (LOQ) calculated using 3.3(SD)/m and 10(SD)/m, where SD is the standard deviation of the blank and m is the slope of the calibration curve, were 33 and 99 ppq, respectively. This ability to detect such ultralow PFAS concentrations demonstrates the exceptional sensitivity of the sensor when MXene-AgNPs10 coating was used. The method was robust and reproducible as indicated by the SD shown in the calibration curve performed for n = 5 independently run experiments (Figure 5B).

In the next step, we assessed the specificity of the sensors, by measuring the response for 1 ppt of various types of PFAS with variable chain lengths, including PFBA, PFBS, PFNS, PFOA, GenX, as well as long carbon chain fatty acids like octanoic acid (OA) and octane-1-sulfonic acid (OSA) that lack C-F bonds in their structure. Additionally, we evaluated the influence of diverse types of salts in the sensor response, ions that are typically present in environmental samples, 1 ppm of PO<sub>4</sub><sup>3-</sup>, Cl<sup>-</sup>, SO<sub>4</sub><sup>2-</sup>, Mg<sup>2+</sup>, KI, KF, as well as HA and 4-DBS. The results are summarized in Figure 5C, along with several

representative structures of the compounds that were analyzed (Figure 5D). The results indicate that the sensor provides quantifiable responses not only to PFOS but also to several other PFAS compounds having long fluorocarbon chains such as PFOA, PFNS, and PFNA (Figure 5C). For PFOA analysis (Figure S6), the impedance responses increase with the increase of PFOA concentration between 0.2 and 1 ppt. For short-chain perfluorinated compounds (i.e., PFHA, PFBS, and GenX), tested at the same concentration (1 ppt), the responses are very low. These findings are in agreement with the results from two previous studies using perfluorinated thiol-modified AuNPs, or single-particle collision electrochemistry using AgNPs, thich have found that only PFAS compounds with relative long perfluoroalkyl chains  $(-CF_2 - \ge 7)$  are able to promote significant F-F interactions. The impedimetric responses for 1 ppt of fluorine-free compounds (OA and OSA) are very small (Figure S7A,B) as compared with 1 ppt of PFHxA (Figure S7C), demonstrating the importance of F-F interactions through the F-rich MXene in addition to the electrostatic binding via the AgNPs. The presence of 1 ppm of PO<sub>4</sub><sup>3-</sup>, F<sup>-</sup>, or SO<sub>4</sub><sup>2-</sup> had a minimum effect in EIS measurements (Figure S7D-F). The impedance response of two other possible interfering compounds, HA and 4-DBS (1 ppm), ranged between 12 and 21% as compared with the response of 1 ppt PFOS (Figure 5C). The sensing stability of the materials was evaluated for several months. For an MXene-AgNPs10 ink stored at RT for 5 months, the sensor response decreased by 18% (Figure S8), which indicates good stability and performance of these materials. We note, however, that when used for PFAS measurements, the sensors will likely require calibration in the testing environment.

Altogether, these results demonstrate extremely low detection limits and the ability of the MXene–AgNP sensor to measure long-chain PFAS compounds. The detection sensitivity of this method (33 ppq for PFOS) is below those of other reported electrochemical sensors (Table S2), demonstrating the potential of this material and sensing technology to meet the requirements for PFAS measurements in aqueous environments. The high sensitivity makes these sensors promising candidates for the direct cost-effective detection of the PFAS content in aqueous samples using a straightforward and inexpensive procedure.

Real Sample Analysis. The ability of the MXene-AgNPs10 sensor to measure PFOS in real samples was also evaluated. Two industrial water samples obtained from a wastewater plant were analyzed with this sensor, and the results were compared with the conventional LS/MS/MS. Since the PFOS concentration in the samples is high, to bring their content to the ppq/ppt levels within the range of the calibration curve, the samples were diluted (1:1000) in PBS before analysis. The comparative results obtained side-by-side with the sensor and LC/MS/MS are summarized in Table S3. For Sample 1, the measured concentration was  $3.87 \pm 0.64$  ppt (n = 3) by the sensor and 2 ppt by LC/MS/MS, and for Sample 2, the PFOS reading was  $5.92 \pm 1.02$  ppt (n = 3) by the sensor and 4 ppt by LC/MS/MS. The PFOA content determined by LC/MS/MS in water samples was 13 ppt (Sample 1) and 23 ppt (Sample 2). Examining the correlation data for PFOS, the sensor results show slightly higher values when individual readings for PFOS are considered compared to LC/MS/MS. A possible reason is the compounded effect of other PFAS present in the sample, resulting in a cumulative measure of "total" PFAS. In complex multianalyte matrices

such as wastewater, several other effects could influence measurements. For example, PFAS can engage in intermolecular interactions with other PFAS or metals, or compete for the same binding sites, affecting the accuracy of measurements compared to LC/MS/MS, which involves a separation process. Overall, these results are encouraging and demonstrate the potential of MXene—AgNPs as an electrode material for the rapid single-step detection of these substances by electrochemical means. The results also underscore the importance of evaluating the impact of matrix constituents, particularly in mixtures, on the measurement accuracy in the PFAS sensing field. Additionally, more extensive testing with real samples is necessary to advance the applicability of these technologies from pristine laboratory standards to field-relevant samples.

## CONCLUSIONS

These results demonstrate the ability of MXene—AgNP assemblies as effective materials and a nanosensing platform to achieve electrochemical quantification of PFAS in aqueous environments using EIS. The comprehensive characterization of the MXene—AgNP nanocomposite and its interaction with PFAS confirmed the structural integrity, composition, and molecular binding mechanism of PFAS to the 2D hybrid material. Critically, MXene—AgNPs are capable of binding long-chain PFAS substances, inducing concentration-dependent changes in the charge-transfer resistance at the MXene—AgNP-modified electrode, enabling quantification by monitoring the changes in surface impedance upon exposure to PFAS.

Several advancements for the development of electrochemical sensors for PFAS detection are reported in this study. First, the results establish the use of MXene-AgNPs as electrode material in impedimetric sensor design, providing superior sensitivity for PFAS as compared to other reported materials. Second, the results demonstrate specificity of the sensor for long-chain PFAS and no interferences from structurally similar compounds lacking F, small molecules, organic matter, and ions. Third, the detection sensitivity, down to parts per billion (ppq) levels, makes these sensors promising candidates for low-cost screening of aqueous samples, such as drinking water and wastewater. With the increased regulations and need for large-scale testing, there is a need to develop lowcost methods for a rapid evaluation of the PFAS content. While conventional techniques like LC/MS/MS are sensitive, selective, and accurate, the high cost of PFAS analysis, ranging from \$200 to \$500 per sample, is prohibitive for many industries and communities. Fourth, the developed methodology is simple and straightforward, enabling the analysis to be completed within 5 min. Because the sensing material is stabilized as a thin film onto the electrode surface, the method ensures portability and ease-of-use of the developed sensor. We expect that these developments may advance the application of electrochemical sensors for PFAS.

This work focused on establishing proof-of-concept and measurement capabilities for several representative PFAS compounds. Future optimization of the MXene—AgNP concept may be needed for the detection of an extended library of PFAS and their mixtures, the use of other electrode supports, and demonstration of measurements in a broader range of sample types and matrices. Ultimately, we anticipate that with further development this new concept will open new avenues for the development of field-portable sensors that can be used as a measurement tool for rapid screening and analysis of PFAS in environmental water samples and other matrices.

#### ASSOCIATED CONTENT

# **Supporting Information**

The Supporting Information is available free of charge at https://pubs.acs.org/doi/10.1021/acssensors.4c00776.

SEM and EDS images of MXene—AgNPs with different Ag contents; EIS responses of the sensor to PFOA, OA, OSA, and small molecules; adsorption capacity of the MXene—AgNP material; stability of MXene—AgNPs over time; performance of sensors compared to other electrochemical sensors reported in the literature; and real sample analysis data of sensors and LC/MS/MS (PDF)

#### AUTHOR INFORMATION

#### **Corresponding Author**

Silvana Andreescu — Department of Chemistry and Biomolecular Science, Clarkson University, Potsdam, New York 13699, United States; orcid.org/0000-0003-3382-7939; Email: eandrees@clarkson.edu

#### **Authors**

Reem Khan – Department of Chemistry and Biomolecular Science, Clarkson University, Potsdam, New York 13699, United States

Zihni Onur Uygun – Department of Chemistry and Biomolecular Science, Clarkson University, Potsdam, New York 13699, United States; Department of Medical Biochemistry, Faculty of Medicine, Kafkas University, Kars 36100, Turkey

Daniel Andreescu — Department of Chemistry and Biomolecular Science, Clarkson University, Potsdam, New York 13699, United States

Complete contact information is available at: https://pubs.acs.org/10.1021/acssensors.4c00776

#### Notes

The authors declare no competing financial interest.

# ACKNOWLEDGMENTS

This work was supported by the grant NSF-2141017 and the New York State Center of Excellence (CoE) in Healthy Water Solutions (Award C190175) to S.A. Any opinions, findings, and conclusions or recommendations expressed in this material are those of the author(s) and do not necessarily reflect the views of the National Science Foundation or the New York Stat. The authors thank Dr. Michelle Crimi for providing the real samples, the CAARES laboratory at Clarkson University for the analysis of the PFAS content in these samples using LC/MS/MS, and to the Center for the Advanced Materials Processing (CAMP) for help with the SEM/EDS measurements in the BMCL lab at Clarkson University. R.K. gratefully acknowledges HEC Pakistan for supporting her PhD studies at Clarkson University.

## ABBREVIATIONS

4-DBS, 4-dodecyl benzenesulfonic acid; HA, humic acid; HFPO–DA, hexafluoropropylene oxide dimer acid (trade name GenX); OSA, octanesulfonic acid; PFBS, perfluorobutanesulfonic acid; PFHxA, perfluorohexanoic acid; PFHxS, perfluorohexanesulfonic acid; PFNA, perfluoroonanoic acid; PFOA, perfluorooctanoic acid; PFOS, perfluorooctanesulfonic

acid; OA, octanoic acid; LC/MS/MS, liquid chromatography tandem mass spectrometry.

#### REFERENCES

- (1) Fenton, S. E.; Ducatman, A.; Boobis, A.; DeWitt, J. C.; Lau, C.; Ng, C.; Smith, J. S.; Roberts, S. M. Per-and polyfluoroalkyl substance toxicity and human health review: Current state of knowledge and strategies for informing future research. *Environ. Toxicol. Chem.* **2021**, 40 (3), 606–630.
- (2) McDonough, C. A.; Li, W.; Bischel, H. N.; De Silva, A. O.; DeWitt, J. C. Widening the Lens on PFASs: Direct Human Exposure to Perfluoroalkyl Acid Precursors (pre-PFAAs). *Environ. Sci. Technol.* **2022**, *56* (10), 6004–6013.
- (3) (a) O'Hagan, D. Understanding organofluorine chemistry. An introduction to the C–F bond. *Chem. Soc. Rev.* **2008**, 37 (2), 308–319. (b) Cousins, I. T.; DeWitt, J. C.; Glüge, J.; Goldenman, G.; Herzke, D.; Lohmann, R.; Ng, C. A.; Scheringer, M.; Wang, Z. The high persistence of PFAS is sufficient for their management as a chemical class. *Environ. Sci. Process Impacts* **2020**, 22 (12), 2307–2312.
- (4) National Health, Nutrition Examination Survey (US) and National Center for Environmental Health (US); National Report on Human Exposure to Environmental Chemicals; Department of Health and Human Services, Centers for Disease Control and Prevention, 2022, Updated March 2022.
- (5) US EPA. https://www.epa.gov/sdwa/and-polyfluoroalkyl-substances-pfas, 2023.
- (6) Li, F.; Duan, J.; Tian, S.; Ji, H.; Zhu, Y.; Wei, Z.; Zhao, D. Shortchain per- and polyfluoroalkyl substances in aquatic systems: Occurrence, impacts and treatment. *Chemical Engineering Journal* **2020**, 380, No. 122506.
- (7) Rehman, A. U.; Crimi, M.; Andreescu, S. Current and Emerging Analytical Techniques for the Determination of PFAS in Environmental Samples. *Trends Environ. Anal. Chem.* **2023**, *37*, No. e00198.
- (8) (a) Zhu, J.; Yang, B.; Peng, L.; Wu, J.; Hao, H.; Lou, S. Targettriggered double fluorescent biosensors for rapid and sensitive detection of long-chain perfluorinated compounds using DNA probe and lysozyme fiber. *Science of The Total Environment* 2023, 860, No. 160496. (b) Concellón, A.; Castro-Esteban, J.; Swager, T. M. Ultratrace PFAS Detection Using Amplifying Fluorescent Polymers. *J. Am. Chem. Soc.* 2023, 145, 11420–11430, DOI: 10.1021/jacs.3c03125.
- (9) Niu, H. W. S.; Zhou, Z.; Ma, Y.; Ma, X.; Cai, Y. Sensitive Colorimetric Visualization of Perfluorinated Compounds Using Polyethylene Glycol and Perfluorinated Thiols Modified Au Nanoparticles. *Anal. Chem.* **2014**, *86* (9), 4170–4177.
- (10) Young, A. S.; Pickard, H. M.; Sunderland, E. M.; Allen, J. G. Organic Fluorine as an Indicator of Per- and Polyfluoroalkyl Substances in Dust from Buildings with Healthier versus Conventional Materials. *Environ. Sci. Technol.* **2022**, *56* (23), 17090–17099.
- (11) (a) Islam, G. J.; Arrigan, D. W. M. Voltammetric Selectivity in Detection of Ionized Perfluoroalkyl Substances at Micro-Interfaces between Immiscible Electrolyte Solutions. ACS Sensors 2022, 7 (10), 2960–2967. (b) Clark, R. B.; Dick, J. E. Towards deployable electrochemical sensors for per-and polyfluoroalkyl substances (PFAS). Chem. Commun. 2021, 57 (66), 8121–8130.
- (12) Cheng, Y. H.; Barpaga, D.; Soltis, J. A.; Shutthanandan, V.; Kargupta, R.; Han, K. S.; McGrail, B. P.; Motkuri, R. K.; Basuray, S.; Chatterjee, S. Metal-Organic Framework-Based Microfluidic Impedance Sensor Platform for Ultrasensitive Detection of Perfluorooctanesulfonate. ACS Appl. Mater. Interfaces 2020, 12 (9), 10503—10514.
- (13) (a) Hassan, M. K. R.; Andreescu, S. Advances in electrochemical detection methods for measuring contaminants of emerging concerns. *Electrochem. Sci. Adv.* **2022**, *2* (6), No. e2100184. (b) Ibrahim, M. W. H.; Andreescu, S. Sensors for Emerging Water Contaminants: Overcoming Roadblocks to Innovation. *Environ. Sci. Technol.* **2024**, *58*, 2636 DOI: 10.1021/acs.est.3c09889. (c) Ryu, H.; Li, B.; De Guise, S.; McCutcheon, J.; Lei, Y. Recent progress in the

- detection of emerging contaminants PFASs. Journal of hazardous materials 2021, 408, No. 124437.
- (14) (a) Viada, B. N.; Yudi, L. M.; Arrigan, D. W. Detection of perfluorooctane sulfonate by ion-transfer stripping voltammetry at an array of microinterfaces between two immiscible electrolyte solutions. *Analyst* **2020**, *145* (17), 5776–5786. (b) Sahu, S. P.; Kole, S.; Arges, C. G.; Gartia, M. R. Rapid and direct perfluorooctanoic acid sensing with selective ionomer coatings on screen-printed electrodes under environmentally relevant concentrations. *ACS omega* **2022**, *7* (6), 5001–5007.
- (15) Karimian, N.; Stortini, A. M.; Moretto, L. M.; Costantino, C.; Bogialli, S.; Ugo, P. Electrochemosensor for trace analysis of perfluorooctanesulfonate in water based on a molecularly imprinted poly (o-phenylenediamine) polymer. *ACS Sensors* **2018**, 3 (7), 1291–1298.
- (16) Kazemi, R.; Potts, E. I.; Dick, J. E. Quantifying interferent effects on molecularly imprinted polymer sensors for per-and polyfluoroalkyl substances (PFAS). *Anal. Chem.* **2020**, 92 (15), 10597–10605.
- (17) Clark, R. B.; Dick, J. E. Electrochemical sensing of perfluorooctanesulfonate (PFOS) using ambient oxygen in river water. ACS Sensors 2020, 5 (11), 3591–3598.
- (18) Clark, R. B.; Wagner, D. C.; Holden, D. T.; Roberts, J. J.; Zumbro, E.; Goodnight, L.; Huynh, K. T.; Green, R. B.; Grove, J. A.; Dick, J. E. PFAS Electroanalysis in Low-Oxygen River Water Using Electrogenerated Dioxygen. *Environ. Sci. Technol.* **2023**, *57* (51), 21815–21822.
- (19) Glasscott, M. W.; Vannoy, K. J.; Kazemi, R.; Verber, M. D.; Dick, J. E.  $\mu$ -MIP: Molecularly Imprinted Polymer-Modified Microelectrodes for the Ultrasensitive Quantification of GenX (HFPO-DA) in River Water. *Environmental Science & Technology Letters* **2020**, 7 (7), 489–495.
- (20) Lamichhane, H. B.; Arrigan, D. W. M. Electroanalytical chemistry of per- and polyfluoroalkyl substances. *Curr. Opin. Electrochem.* **2023**, *40*, No. 101309.
- (21) Khan, R.; Andreescu, D.; Hassan, M. H.; Ye, J.; Andreescu, S. Nanoelectrochemistry Reveals Selective Interactions of Perfluoroalkyl Substances (PFASs) with Silver Nanoparticles. *Angew. Chem., Int. Ed.* **2022**, *61* (42), No. e202209164.
- (22) Lim, K. R. G.; Shekhirev, M.; Wyatt, B. C.; Anasori, B.; Gogotsi, Y.; Seh, Z. W. Fundamentals of MXene synthesis. *Nature Synthesis* **2022**, *1* (8), 601–614.
- (23) Khan, R.; Andreescu, S. MXenes-Based Bioanalytical Sensors: Design, Characterization, and Applications. *Sensors* **2020**, *20* (18), 5424
- (24) (a) Pei, Y.; Zhang, X.; Hui, Z.; Zhou, J.; Huang, X.; Sun, G.; Huang, W. Ti3C2TX MXene for Sensing Applications: Recent Progress, Design Principles, and Future Perspectives. *ACS Nano* **2021**, *15* (3), 3996–4017. (b) Rizwan, K.; Rahdar, A.; Bilal, M.; Iqbal, H. M. N. MXene-based electrochemical and biosensing platforms to detect toxic elements and pesticides pollutants from environmental matrices. *Chemosphere* **2022**, *291*, No. 132820.
- (25) Guo, J.; Peng, Q.; Fu, H.; Zou, G.; Zhang, Q. Heavy-Metal Adsorption Behavior of Two-Dimensional Alkalization-Intercalated MXene by First-Principles Calculations. *J. Phys. Chem. C* **2015**, *119* (36), 20923–20930.
- (26) Dixit, F.; Munoz, G.; Mirzaei, M.; Barbeau, B.; Liu, J.; Duy, S. V.; Sauvé, S.; Kandasubramanian, B.; Mohseni, M. Removal of Zwitterionic PFAS by MXenes: Comparisons with Anionic, Nonionic, and PFAS-Specific Resins. *Environ. Sci. Technol.* **2022**, *56* (10), 6212–6222.
- (27) Le, T.; Jamshidi, E.; Beidaghi, M.; Esfahani, M. R. Functionalized-MXene Thin-Film Nanocomposite Hollow Fiber Membranes for Enhanced PFAS Removal from Water. ACS Appl. Mater. Interfaces 2022, 14 (22), 25397–25408.
- (28) Ma, J.; Wang, Y.; Xu, H.; Ding, M.; Gao, L. MXene (Ti3T2CX)-reinforced thin-film polyamide nanofiltration membrane for short-chain perfluorinated compounds removal. *Process Safety and Environmental Protection* **2022**, *168*, 275–284.

ı

- (29) Wang, L.; Jiang, H.; Wang, H.; Show, P. L.; Ivanets, A.; Luo, D.; Wang, C. MXenes as heterogeneous Fenton-like catalysts for removal of organic pollutants: A review. *J. Environ. Chem. Eng.* **2022**, *10*, No. 108954.
- (30) Matsugi, M.; Curran, D. P. Reverse fluorous solid-phase extraction: A new technique for rapid separation of fluorous compounds. *Org. Lett.* **2004**, *6* (16), 2717–2720.
- (31) Tan, X.; Sawczyk, M.; Chang, Y.; Wang, Y.; Usman, A.; Fu, C.; Král, P.; Peng, H.; Zhang, C.; Whittaker, A. K. Revealing the molecular-level interactions between cationic fluorinated polymer sorbents and the major PFAS pollutant PFOA. *Macromolecules* **2022**, 55 (3), 1077–1087.
- (32) Erkal, T. S.; Shamsuddin, N.; Kirmizialtin, S.; Yazaydin, A. O. Computational investigation of structure–function relationship in fluorine-functionalized MOFs for PFOA capture from water. *J. Phys. Chem. C* 2023, 127 (6), 3204–3216.
- (33) Lazanas, A. C.; Prodromidis, M. I. Electrochemical Impedance Spectroscopy—A Tutorial. ACS Meas. Sci. Au 2023, 3 (3), 162–193.
- (34) Alhabeb, M.; Maleski, K.; Anasori, B.; Lelyukh, P.; Clark, L.; Sin, S.; Gogotsi, Y. Guidelines for Synthesis and Processing of Two-Dimensional Titanium Carbide (Ti3C2Tx MXene). *Chem. Mater.* **2017**, 29 (18), 7633–7644.
- (35) Zou, G.; Zhang, Z.; Guo, J.; Liu, B.; Zhang, Q.; Fernandez, C.; Peng, Q. Synthesis of MXene/Ag Composites for Extraordinary Long Cycle Lifetime Lithium Storage at High Rates. ACS Appl. Mater. Interfaces 2016, 8 (34), 22280–22286.
- (36) Uygun, Z. O.; Sezgintürk, M. K. A novel, ultra sensible biosensor built by layer-by-layer covalent attachment of a receptor for diagnosis of tumor growth. *Anal. Chim. Acta* **2011**, 706 (2), 343–348.
- (37) Wang, Y.; Wang, S.; Dong, N.; Kang, W.; Li, K.; Nie, Z. Titanium Carbide MXenes Mediated In Situ Reduction Allows Label-Free and Visualized Nanoplasmonic Sensing of Silver Ions. *Anal. Chem.* **2020**, 92 (6), 4623–4629.
- (38) Naguib, M.; Kurtoglu, M.; Presser, V.; Lu, J.; Niu, J.; Heon, M.; Hultman, L.; Gogotsi, Y.; Barsoum, M. W. Two-Dimensional Nanocrystals Produced by Exfoliation of Ti3AlC2. *Adv. Mater.* **2011**, 23 (37), 4248–4253.
- (39) Veljović, D. N.; Gurešić, D. M.; Jokić, A. B.; Vasić, V. M.; Laban, B. B. Solid-State Synthesis of Silver Nanoparticles and Their Catalytic Application in Methylene Blue Reduction. *ChemistrySelect* **2020**, *5* (34), 10488–10494.
- (40) Vara, J. A.; Dave, P. N.; Chaturvedi, S. The catalytic activity of transition metal oxide nanoparticles on thermal decomposition of ammonium perchlorate. *Defence Technology* **2019**, *15* (4), 629–635.
- (41) Gao, Y.; Gou, W.; Zeng, W.; Chen, W.; Jiang, J.; Lu, J. Determination of Perfluorooctanesulfonic acid in water by polydopamine molecularly imprinted /Gold nanoparticles sensor. *Microchemical Journal* **2023**, *187*, No. 108378.
- (42) Uygun, Z. O.; Uygun, H. D. E. A short footnote: Circuit design for faradaic impedimetric sensors and biosensors. *Sens. Actuators, B* **2014**, 202 (31), 448–453.